Scattering Effects of Traveling Wave Currents on Linear Features

Donald Hilliard
Advanced Research & Technology Corp.
Camarillo, CA, USA
dhilliard@artc-net.com

Tai Kim
Naval Air Weapons Center
Point Mugu, CA, USA
tai.kim@navy.mil

Dean Mensa
Engility Corp.
Camarillo, CA, USA
dmensa@roadrunner.com

Abstract- RCS images are used to locate and characterize scattering features on complex objects. While imaging systems faithfully locate point-source features, they fail to accurately portray features associated with traveling-wave and multiple-reflection effects. The behavior of traveling-wave scattering is analyzed from analytic considerations and experimental data. In spite of its relative simplicity, a slender metallic body is used to illustrate the difficulty of separating traveling-wave scattering from other features.

INTRODUCTION

The utility of RCS images for determining the source and nature of scattering features has been demonstrated and widely used to characterize and modify the object's radar signature. The signal processing required to form an image uses frequency and angle responses of the object under test to extract the location and magnitude of point scatterers whose collective responses constitute the observed data. The frequency/angle data are decomposed into basis functions describing the responses to independent point scatterers. For objects exhibiting other basis functions, such as those for traveling-wave scattering, ISAR images reveal unexpected results that can obscure proper interpretation of the scattering mechanism. Backscattered responses of extended objects irradiated near grazing incidence exhibit unique characteristics caused by backward-traveling currents that induce fields radiated toward the source, known as "traveling-wave" responses. Currents reflected from the body's far end produce backward traveling currents which cause radiation toward the source. Consequently, observed responses of even relatively simple objects can include combinations of scattered and "traveling-wave" effects thus precluding clear diagnoses of underlying scattering mechanisms. Because traveling-wave lobes occur for limited frequency-dependent grazing angles, localizing their effects from high-resolution images can be elusive. Specifically, traveling-wave responses are not readily distinguished from direct and diffracted responses observed in the image. The paper deals with backscattering data collected on a slender metallic rod with polarization parallel to the plane of incidence, intended to exhibit effects of traveling waves for the rod's grazing angles.

In spite of its relatively simple geometry, the linear rod presents complicated responses owing to the combined effects of scattered, diffracted, and traveling-wave effects. We begin with a review of the cause of traveling-wave behavior.

CURRENT SOURCE WITH UNIFORM AMPLITUDE AND LINEAR PHASE

Figure 1 shows a filamentary linear conductor of length L carrying a current $I_0 e^{-jkz}$, where z is the coordinate along the line. Current elements along the line have uniform magnitude I_0 and phase varying linearly with z, which constitutes a traveling wave current in the z direction.

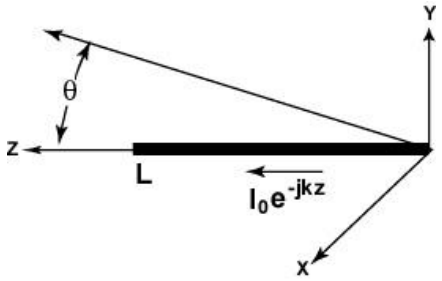

Figure 1. Filamentary line source with uniform amplitude and linear phase.

The radiated far field is given by:

$$E(\theta) = Io[exp(-jkr)/4\pi r]\ [sin(\theta)]L\ [sin(u)/u] \qquad (1$$

where $u = kL/2[1-cos(\theta)]$

Figure 2 shows the far-field radiation pattern for the 10λ line; the principal radiation lobe is slightly offset from the line axis and its width is inversely proportional to the line length.

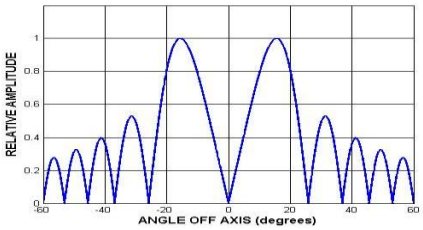

Figure 2. Normalized radiation pattern for 10λ line current source with linear phase.

The offset radiation angle results from the product of the *sin(θ)* and *sin(u)/u* terms which describe the radiation from the product of the two terms which constitute the pattern of the current element and the array factor, respectively. While the latter term peaks along the axis, the former peaks in a direction normal to the axis and falls to zero along the axis. The product, therefore, peaks at an intermediate angle. The principal response, known as the traveling-wave lobe, is due to the current traveling along the axis. Figure 3 illustrates the response formed by the product of the element pattern and the array factor. Radiation along the axis is zero and the angle of maximum radiation deviates from the line axis as the line length decreases. The antenna radiation peak describes a cone offset from the axis by the traveling wave lobe angle.

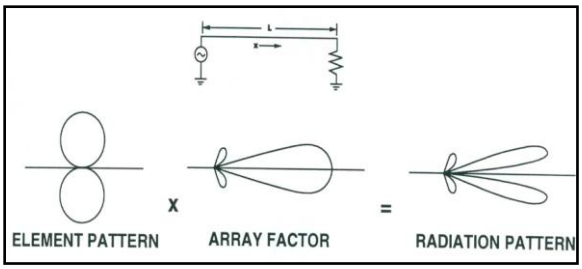

Figure 3. Radiation pattern of traveling-wave antenna

RADAR CROSS SECTION ANALYSIS AND IMAGING THE TRAVELING WAVE

We next consider the apparent location of the backscattering source associated with the traveling wave from the perspective of a monostatic coherent radar measurement. The apparent location of the backscattering source is indicated on down-range profiles and two-dimensional Inverse Synthetic Aperture Radar (ISAR) images. The former are obtained by processing wide-band scattering responses; the latter by processing wide-band, wide-angle scattering responses. The wide-band processing produces the effective range of the scattering source by accounting for the round-trip signal phase as a function of frequency. Cross-range information is derived from the changing phase as a function of angle.

Figure 4 represents a backscatter measurement of a filamentary conductor with the current at the near end used as a phase reference.

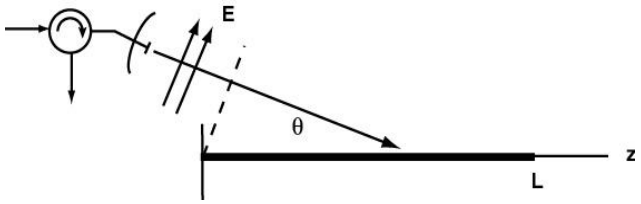

Figure 4. Backscatter measurement of a filamentary conductor.

The elemental backscattered field radiated by a current component at location *z* is proportional to the current reflected toward the source by the reflection coefficient

$$\Delta E_s(\theta) \propto \Gamma E \sin(\theta)\, e^{-jk[L\cos(\theta)+(L-z)+z\cos(\theta)]} \qquad (2$$

The first term in the brackets represents the *E* field propagation distance from the origin to the end of the conductor, the second term represents the distance traveled along the axis by the reflected current along the axis, and the third term represents the propagation distance to the origin. The various terms are indicated in figure 5.

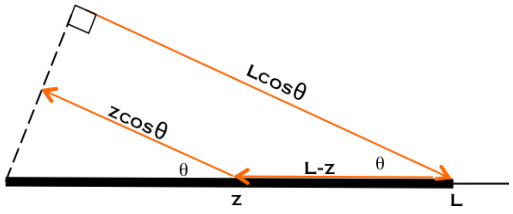

Figure 5. Round Trip Backscatter Phase Components.

The total backscattered field is the integral of the elemental fields over the total length *L*.

$$E_s(\theta) = \int_{Z=0}^{L} \Gamma E \sin(\theta) e^{-jk[L\cos(\theta)+(L-z)+z\cos(\theta)]} dz \qquad (3$$

The round-trip phase of the scattered field is obtained by performing the integral indicated by (3, rewritten as:

$$E_s(\theta) = \Gamma E sin(\theta) e^{-jkL[1+cos(\theta)]} \int_{Z=0}^{L} e^{jkz[1-cos(\theta)]} dz \quad (4$$

The integral is evaluated by letting $a = [1\text{-}cos(\theta)]$, then:

$$\int_{Z=0}^{L} e^{jkaz} dz = \frac{1}{jku} e^{(jkaL-1)} \quad (5$$

Algebraic manipulations yield:

$$\int_{Z=0}^{L} e^{jkaz} dz = L e^{jk\frac{L}{2}} \left(\frac{sin\left(ka\frac{L}{2}\right)}{ka\frac{L}{2}} \right) \quad (6$$

Using (6, expression (4 can be written as :

$$E_s(\theta) = e^{-jkL[1+cos(\theta)]} e^{jk\frac{L}{2}a} \Gamma EL sin(\theta) \left(\frac{sin\left(k\frac{L}{2}a\right)}{k\frac{L}{2}a} \right) \quad (7$$

The two exponential terms and the remaining terms describe the phase and magnitude of the scattered signal, respectively. Figure 6 shows the magnitude of the backscattered field resulting from the backward-traveling wave current versus grazing angle as a function of wire length *L*, in wavelengths, ranging from 5 to 25.

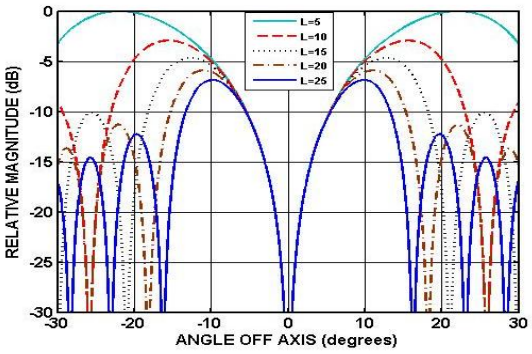

Figure 6. Backscattered field pattern resulting from backward traveling-wave current.

To confirm the backscattered magnitude of the traveling wave response, results of measurements at 4 GHz on a slender rod 0.64 cm (0.25 inch) in diameter and 183 cm (6ft) in length, with the radar electric field parallel to the plane containing the rod axis (HH polarization in this case), are shown in Figure 7. The faint (red) curve is the raw RCS and the bold (blue) curve is the mean RCS, which is determined by performing an average over a 5° aspect angle window and sliding the window every 1° across the entire range of aspect angles (5° window, 1° slide). The 4 GHz RCS response of the 24.4λ rod shows traveling-wave responses peaking at 10°, which correlates with results of Figure 6 for a 25λ rod. Figure 7 shows the RCS component of the traveling wave with amplitude about 12 dB below the rod's peak broadside response and about 23 dB above the mean value of the rod's other diffraction terms.

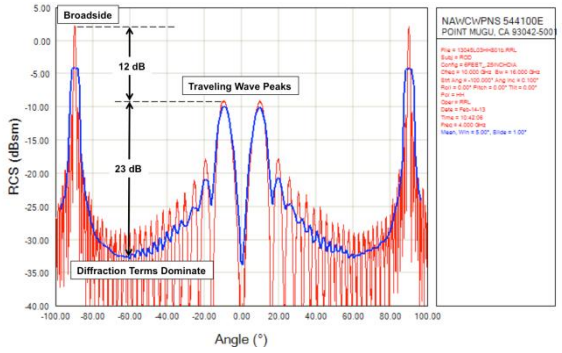

Figure 7. CW response of 24.4λ rod for 4 GHz.

The total phase of (7 provides the relative range information of the traveling wave scattering source. The sin(.)/(.) term provides the amplitude aspect angle envelope, but because it is a real function, its phase contribution is zero. Therefore, the total signal phase may be simplified to:

$$\phi_T = -\frac{kL}{2[1+3cos(\theta)]} \quad (8$$

The spatial location of scattering elements in ISAR images is determined by the phase variations as a function of wavenumber *k* and viewing angle θ. The down range, *R*, and cross-range, *XR*, coordinates in the image are proportional to the instantaneous phase rate of change with respect to *k* and θ, respectively according to:

$$R = \frac{1}{2}\left(\frac{\partial \phi_T}{\partial k}\right) \quad and \quad XR = \frac{1}{2k_0}\left(\frac{\partial \phi_T}{\partial \theta}\right) \quad (9$$

where the factor of *(1/2)* accounts for the round trip distance and k_0 is the average wavenumber used to determine the cross range coordinate.

For θ=0, the round-trip phase corresponding to the conductor end is *2kL*. The down range scatterer location relative to the front of the rod is $R = L$. However, because

there is no current induced on the conductor for θ=0, the preceding observation is meaningless. As θ increases, the range of the conductor rear end is $Lcos(\theta)$ while the effective range of the traveling wave, given by (8, is $(L/4)[1+3cos(\theta)]$. The effective range of the traveling wave response projects past the rear end of the conductor; for small angles corresponding to long conductors, however, the difference is minor.

To facilitate comparisons with experimental results, it is convenient to define the origin of the coordinate system, shown in figure 11, coincident with the center of the rod and center of rotation for the measurements. For the case shown, the round-trip distance corresponding to point z is:

$$r = (L/2)\cos(\theta) + [(L/2)-z] + z\cos(\theta) \qquad (10$$

The first term indicates the free-space distance traveled by the incident wave from the origin to the far end; the second term indicates the distance traveled by the current from the far end to the point z; the third term indicates the distance traveled by the wave radiated from point z to the origin.

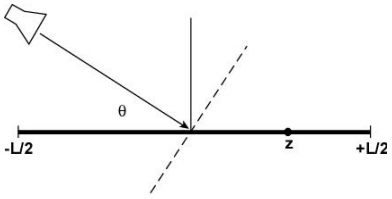

Figure 11. Coordinate system with origin at rod center

The effect of shifting the coordinate system origin is determined by inserting the distance r into (3 and integrating from $-L/2$ to $+L/2$.

The preceding section considered the first-order response of traveling-wave scattering, but ignored higher order diffraction terms from the ends of the rod. When scattering features of linear conductors are observed in experimental radar images, some peculiar responses are noted and addressed in the following section. Figure 12 show symbolic representations of ISAR images of key scattering mechanisms for a linear rod of length L viewed at aspect angle incidence, θ, shown as 30°. All the mechanisms shown, functions of frequency and aspect angle, appear simultaneously in an ISAR image. The solid dots represent the apparent location of several scattering features observed by a radar represented by the transmit/receive antenna at the bottom of each figure.

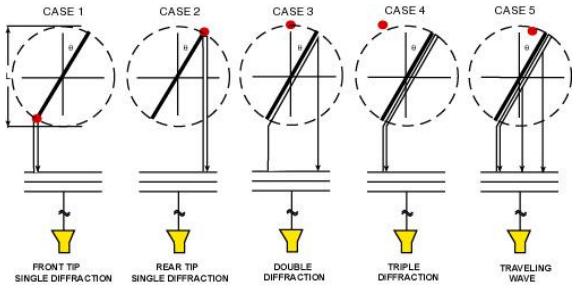

Figure 12. Scattering mechanisms of the rod for 30 ° oblique incidence.

Figure 13 shows a Global RCS response in which frequency and viewing angle are plotted on the radial and angular coordinates, respectively. The frequency ranges from 2 GHz on the inner circle to 10 GHz on the outer circle and the angle from -90° to +90°, where 0 is along the rod axis. The plot shows the prominent traveling-wave response for angles decreasing with frequency. In order to facilitate further analysis, we focus on 4 GHz for detailed examination. Figure 14 shows another version of the Global RCS plot with a slightly different scale from 3 to 8 GHz with a 4 GHz polar plot shown in the center and a corresponding black circle in the Global RCS plot.

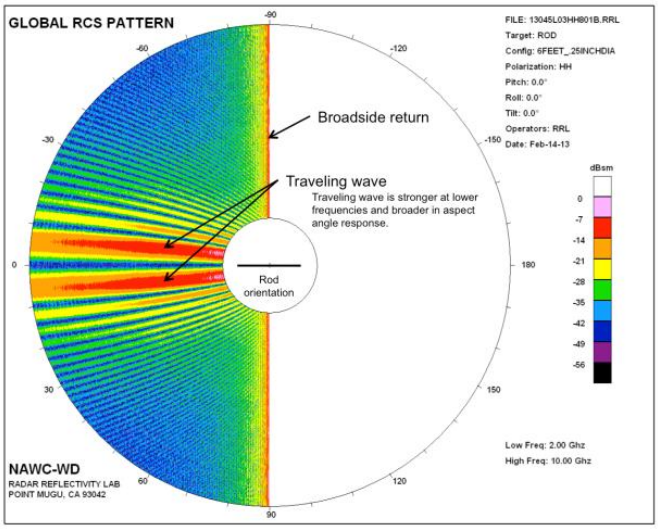

Figure 13. Global RCS response of rod from 2 to 10 GHz

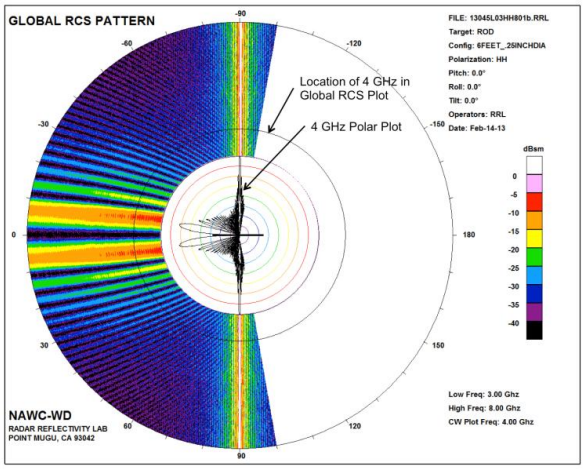

Figure 14. Global RCS of rod from 3 to 8 GHz with polar plot at center.

The Global Range plot provides a capability to assess scatterer down range locations with aspect angle by Fast Fourier Transform (FFT) processing RCS data over sufficiently wide frequency band to render good resolution. Figure 15 shows a Global Range plot obtained by processing data from 3 to 6 GHz. The RCS scale was adjusted in order to resolve the front tip and triple diffraction scatterers, but as a result the scale maximum is low, which clips the traveling wave peak level preventing comparing it to the diffraction terms in this plot. The relative range in the plot is on the radial coordinate from -2m on the inner circle to +2m on the outer circle with 0 range coinciding with the center of rotation. The angular coordinate of 0 corresponds to the rod axis. Four distinct curved responses are evident. The front tip single diffraction is shown by the outer trace. The rear tip single diffraction is shown by the second trace. The double diffraction (near/far/receiver) is shown by the third trace from the outer limit and appears at a constant range offset from the outer limit and appears at a constant range offset from the center by half the rod length. At near grazing aspect angles up to about 10 degrees, the rear single, double, and triple diffraction terms blend together with the traveling wave; all four mechanisms are contained within the same range cell at grazing angles.

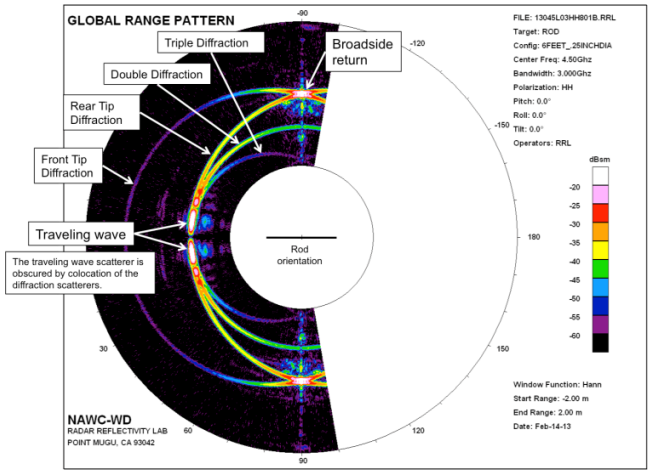

Figure15. Global RCS range response of the rod.

The ISAR image provides a capability to identify scatterer spatial locations in more detail with a two-dimensional map of down range and cross range locations at specific aspect angles of the rod. The ISAR image is produced by FFT processing RCS data over sufficiently wide frequencies and aspect angles to render good resolution. For the ISAR images shown below, aspect angle processing limited to 14.3° in order to avoid cross-range smearing of the rear scatterers, which happens because of their delayed phase characteristics as previously described. Limiting the aspect angle processing to 14.3° limits the frequency processing to 1 GHz in order to have the same cross-range and down-range scales. As a result, the down-range resolution in these images is 15cm (6in) , three times less than the resolution for the Global Range plot above, which has a bandwidth of 3 GHz and resolution of 5cm (2in). As shown below, 15cm resolution is insufficient to resolve the traveling wave from diffraction terms range locations. As in the case for the Global Range plot, the ISAR RCS scale is low in order to resolve the front tip and triple diffraction terms at the consequence of clipping the traveling wave peak in the third image below, thus preventing level comparisons.

Figure 16 shows an ISAR image obtained by processing data from a bandwidth of 1 GHz centered on 4 GHz and for a 14.3° aspect angle centered on 50° from the rod axis. The black line indicates the location

of the rod. In this case the traveling wave is not present, but the four diffraction terms are clearly separated as they were in the Global Range plot at the same aspect angle. At 30° aspect angle from end on, shown in Figure 17, the rear diffraction terms are seen to merge. At 10° aspect angle from end on, shown in Figure 18, the traveling wave arises and is joined by the rear diffraction terms. Although the down- range locations of the rear scattering terms are not resolvable, they are slightly differentiated in cross range.

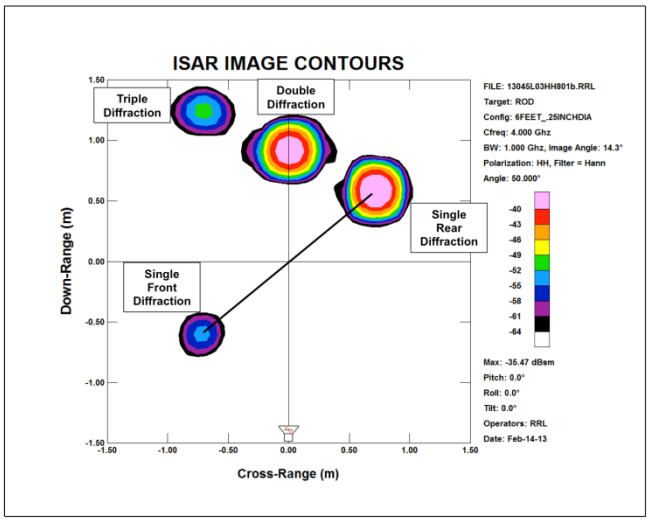

Figure 16. ISAR image of rod at 50 degrees aspect angle.

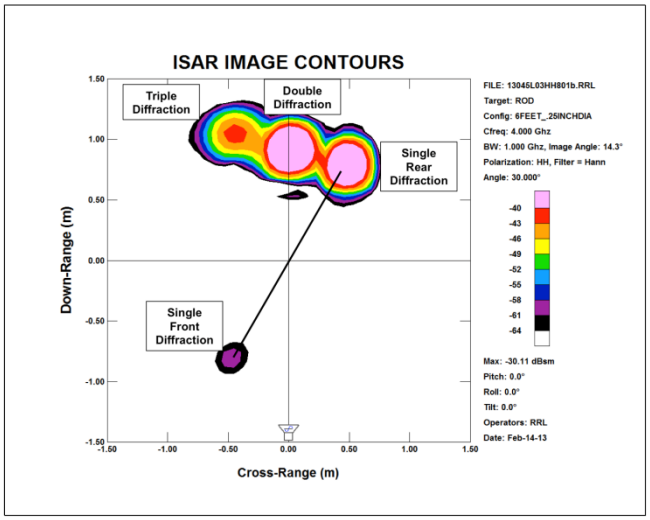

Figure 17. ISAR image of rod at 30 degrees aspect angle.

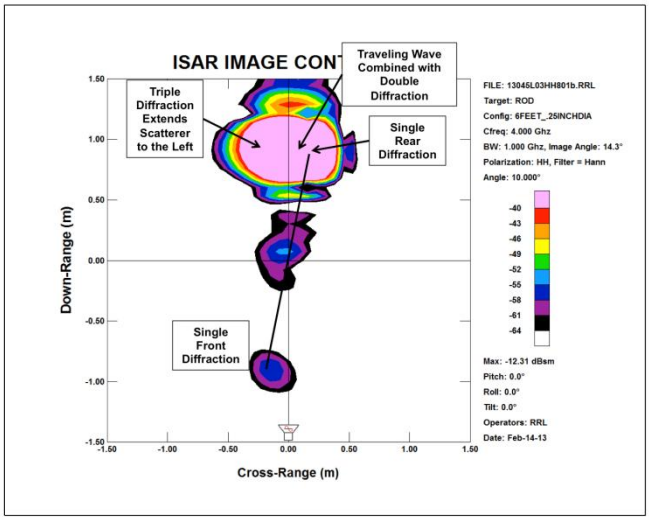

Figure 18. ISAR image of rod at 10 degrees aspect angle.

SUMMARY

The preceding analyses showed the physical attributes of monostatic RCS behavior observed for extended objects arising from traveling wave and diffraction scattering mechanisms. Because the imaging process is based on single scattering from point objects, apparent locations of the more complex features are rendered displaced from the physical locations of the scattering sources. In particular, scattering sources associated with single diffraction are rendered in their physical location while scattering sources associated with multiple diffractions and traveling wave effects are rendered in displaced locations. The presence of these effects obscures the diagnosis of scattering features normally inferred from range profiles and ISAR images. The examples shown indicate that observed scattering responses, even for a simple object such as a linear rod, can be relatively complex and not readily interpreted.

REFERENCES

1. S. Ramo, J. Whinnery, T. VanDuzer, *Fields and Waves in Communication Electromagnetics*, ,John. Wiley and Sons, New York, 1965, pp. 646-648.
2. R. Plonsey, R. Collins, *Principles and Applications of Electromagnetic Fields*, McGraw- Hill, New York, 1961, pp. 394-395.
3. W. Stutzman, G.Thiele, *Antenna Theory and Design*, John Wiley and Sons, New York, 1981, pp.17-26.